# Photodegradation of methylene blue catalyzed by tungstophosphate/aerogel hybrid materials under ultraviolet irradiation

Fatima Yahya[a], Houssam El-Rassy[b],*, Ghassan Younes[a], Rami Al-Oweini[a,c,]*

[a]_Department of Chemistry, Faculty of Science, Beirut Arab University, P.O. Box: 11 50 20, Riad El Solh, 1107 2809, Beirut, Lebanon, Tel. +961 7 985 858, Ext: 3316, Lab: 3379; Fax: +961 7 985 858, Ext: 3302; emails: roweini@aub.edu.lb (R. Al-Oweini), fatima-yahya-yahya@hotmail.com (F. Yahya), ghass@bau.edu.lb (G. Younes)_
[b]_Department of Chemistry, American University of Beirut, P.O. Box: 11-0236, Riad El-Solh 1107 2020, Beirut, Lebanon, email: he13@aub.edu.lb (H. El-Rassy)_
[c]_Present address: Kamal A. Shair Central Research Science Laboratory, Faculty of Arts and Sciences, American University of Beirut, P.O. Box: 11-0236, Riad El-Solh 1107 2020, Beirut, Lebanon_

## ABSTRACT

In this study, the tungstophosphates structural-family series ($PW_9$, $P_2W_{12}$, $P_2W_{15}$, $P_2W_{18}$, $P_4W_{24}$, $P_5W_{30}$, $P_6W_{18}$, and $P_8W_{48}$) were successfully immobilized onto silica aerogels (tetraethyl orthosilicate aerogel, TEOS) via a facile reaction method, under mild conditions. The chemical and structural properties of the prepared hybrid materials were assessed by various techniques such as Fourier transform infrared spectroscopy (FTIR), thermal gravimetric analysis, and X-ray diffraction. Additionally, FTIR, UV-visible (UV-Vis), Brunauer–Emmett–Teller, scanning electron microscopy, and energy-dispersive X-ray techniques eased our understanding for the loading of polyoxometalates (POMs) and their distributions onto the surface of silica aerogels. The most important analysis, in this study, is the nitrogen adsorption–desorption technique that showed a significant increase in the specific surface area and pore volume of the hybrid catalysts after the immobilization in comparison to the pristine POM counterparts, thus enhancing the probability of the surface-active sites. The photocatalytic activities of these photocatalysts were tested toward the cationic Methylene Blue dye model (MB) under ultra-violet light irradiation. The results obtained by UV-Vis and MS analyses confirmed that the MB can be removed by the prepared photocatalysts with maximum degradation efficiency of 75%–95% and 90%–98% in 120 min, for POMs and POM-TEOS hybrids, respectively.

_Keywords:_ Polyoxometalates; Silica aerogels; Immobilization; Hybrid catalysts; Methylene Blue; Photocatalytic degradation

## 1. Introduction

Organic dyes are widely used in various industrial fields such as in textile, leather tanning, food industries, and plastics, all of which may contaminate water, upon waste disposal, with serious environmental problems [1,2]. Also, such industries would cause carcinogenic problems to humans due to their toxicities generated from dyeing paper, paints, and silk textiles [3]. In addition, 15% of dyes are released from the effluent of textiles during the process of dyeing [4]. Accordingly, it is urgent to find an efficient solution for the organic dyes in wastewater before springing it back into nature. Methylene blue, an aromatic dye, is usually used as a model reaction in order to study the photocatalytic effects due to the apparent disappearance of its blue color during the photocatalytic degradation [5]. Alternatively, the most important part of photocatalysis is the detection of intermediate products and the different proposed degradation mechanism pathways [6–8]. The main and only controversy is about the degradation of the dye taking place

* Corresponding authors.

either at the central aromatic ring or at the methyl group on the benzene ring [9].

Polyoxometalates (POMs) are a family of discrete metal oxide frameworks characterized by controllable size and shape [10–17]. They possess various compelling properties that make them chemically attractive in redox reactions and especially in oxidation reactions for homogeneous and heterogeneous systems, as well as having strong acidity surfaces exhibiting oxo groups with highly negative charges [18]. Interestingly, POMs became the main focus of attention in recent chemical research due to their novel molecular and structural compositions making them more chemically reactive and attractive [19–33].

Furthermore, POMs are highly soluble in water and as such are difficult to be separated from the solution mixture, as well as having low surface areas [34]. In order to overcome these barriers, the immobilization of POMs onto porous materials and solid supports like titania [35], silica [36], zirconia [37], and activated carbon [38], thus creates highly mesoporous hybrid composites, as insoluble and heterogeneous catalysts for environmental applications, exhibiting good adsorption activity [19–21].

We report herein the immobilization of phosphorus-based POMs family ($Na_9[\alpha$-$PW_9O_{34}]\cdot7H_2O$, $PW_9$; $K_{12}[\alpha$-$H_2P_2W_{12}O_{48}]\cdot24H_2O$, $P_2W_{12}$; $Na_{12}[\alpha$-$P_2W_{15}O_{56}]\cdot24H_2O$, $P_2W_{15}$; $K_6[\alpha$-$P_2W_{18}O_{62}]\cdot14H_2O$, $P_2W_{18}$; $K_{16}Li_2[H_6P_4W_{24}O_{94}]\cdot33H_2O$, $P_4W_{24}$; $K_{12.5}Na_{1.5}[NaP_5W_3O_{110}]\cdot15H_2O$, $P_5W_{30}$; $Na_{20}[P_6W_{18}O_{79}]\cdot37.5H_2O$, $P_6W_{18}$; and $K_{28}Li_5[H_7P_8W_{48}O_{184}]\cdot92H_2O$, $P_8W_{48}$) onto silica aerogels (TEOS). The prepared materials were used as efficient heterogeneous catalysts for the photodegradation of Methylene Blue (MB) in aqueous solutions under ultra-violet light irradiation. The prepared photocatalysts were characterized by Fourier transform infrared spectroscopy (FTIR), UV-visible spectroscopy (UV-Vis), powder X-ray diffraction (XRD), scanning electron microscopy (SEM), energy-dispersive X-ray spectroscopy (EDX), nitrogen sorption Brunauer–Emmett–Teller studies (BET), atomic absorption spectroscopy (AAS), thermal gravimetric analysis (TGA), and mass spectrometry (MS). Based on our UV-Vis analyses and the obtained MS results, we report a proposed mechanism for the photocatalyic degradation of MB.

## 2. Materials and methods

In this work, all reagents and solvents used for the syntheses of the hybrid materials were purchased from Merck (Germany), Sigma-Aldrich (Germany), Acros Organics (Belgium), Fluka (Germany), Alieh (Lebanon), Alpha Chemika (India), and Himedia (India). Specifically, methylene blue ($C_{16}H_{18}ClN_3S\cdot3H_2O$) was supplied by Merck (Germany). All chemicals were used as received without further purification. In addition, double distilled water and deionized water were freshly prepared in the lab.

### 2.1. Preparation of heteropolytungstates and silica aerogels

Primarily, the the used heteropolytungstates (Fig. 1) were synthesized according to known methods in the literature [39,40]. On the other hand, silica aerogels were prepared according to our previous work [33,41,42]. Typically, the synthesis of TEOS aerogels was carried out in two steps of a sol–gel
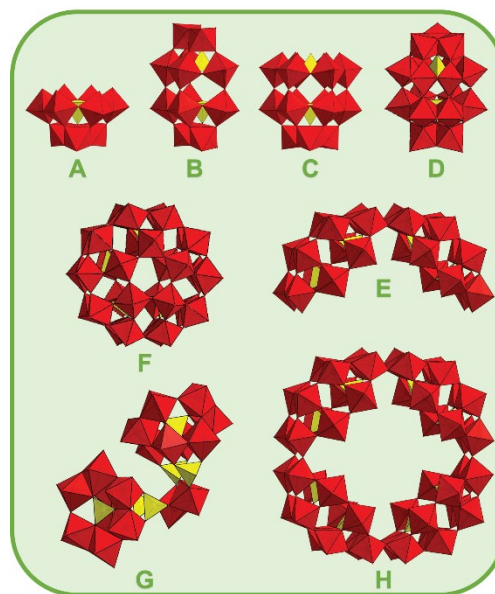


Fig. 1. Polyhedral representation of the used POMs. (A) $PW_9$, (B) $P_2W_{12}$, (C) $P_2W_{15}$, (D) $P_2W_{18}$, (E) $P_4W_{24}$, (F) $P_5W_{30}$, (G) $P_6W_{18}$, and (H) $P_8W_{48}$. Color code, polyhedra: $WO_6$ (red), $PO_4$ (yellow).

process comprising of hydrolysis and condensation, followed by $CO_2$ supercritical drying. The final and optimized molar ratios of reagents used were $Si$–$(OC_2H_5)_4$ (1 M), methanol (12 M), $H_2O$ (6 M), HCl ($3 \times 10^{-3}$ M), and $NH_3$ ($6 \times 10^{-3}$ M).

### 2.2. Immobalization of heteropolytungstates onto the surface of silica aerogels

The procedure of POM immobilization onto the surface of TEOS aerogels followed a typical method described by Al-Oweini et al. [33], where 0.25 g of each POM was added to 0.5 g of TEOS aerogels in 35 mL of methanol, the mixture was then kept under reflux for 3 h, which was later filtered and washed with methanol, and finally the desired product was dried under vacuum.

### 2.3. Characterization

#### 2.3.1. Material properties

The characterization of the prepared hybrid photocatalysts were characterized by FTIR spectroscopy (Nicolet-Avatar 370, United States) in the range 400–4,000 cm$^{-1}$ to confirm purity of the prepared samples in comparison to literature data. XRD patterns were recorded on a BRUKER (Germany) D8 advance X-ray diffractometer, employing Cupper $K_\alpha$ radiation ($\lambda$ = 1.5418 Å). TGA was obtained on a BRUKER (Germany) TGA-IR TENSOR 27 NETZSCH TG 209 F1 LIBRA in order to confirm the chemical and structural properties of the catalysts. The elemental content of tungsten in the catalysts was performed using a SOLAAR atomic absorption spectrophotometer with ASX-510. Additionally, SEM images and EDX spectra were obtained on a MIRA3 LMU equipped with an OXFORD (England) EDX detector by TESCAN (Czech Republic) to improve the morphology

and the percentage by atoms of the elements present in the hybrid catalysts. The most important technique used was the Nitrogen adsorption–desorption studies, performed on a BET NOVA 2200 automated surface area and probe size analyzer with NOVA AWIN2 software, to assess the loading distribution of the POMs onto the surface of the TEOS aerogels, which provided additional information like the surface area, pore size, and pore volume.

### 2.3.2. Photocatalytic activity

The photodegradation reactions were performed under ultraviolet irradiation (mercury lamp 100 W, 254 nm) in a photochemical reactor (ACE Glass). The aqueous solution of MB (50 mL, $2.975 \times 10^{-5}$ M) was placed in a quartz tube inside the photoreactor and the hybrid materials (75 mg) were added with continuous stirring to ensure the uniform homogeneity of the solution. At a 15 min time interval, 1 mL aliquot was collected and centrifuged in order to remove any precipitate. Then, the filtrate was analyzed using the UV-Vis spectroscopy where the variations at maximum wavelength (665 nm) were recorded. This process was repeated three times to test the reliability and reproducibility of the measurements at the same conditions, and complete results are presented in Fig. S1 and Table S1.

## 3. Results and discussion

### 3.1. Physicochemical properties of POMs/TEOS hybrid materials

#### 3.1.1. Infrared spectroscopy

The FTIR spectra in Figs. S2–S9 of the prepared catalysts revealed the existence of the characteristic bands at 1,080, 982, 890, and 796 cm$^{-1}$ assigned to P-O$_a$, W-O$_t$, P-(W-O$_b$-W), and (W-O$_c$-W) vibrations, respectively, that are relevant to the POMs [10–12]. Furthermore, the characteristic bands of the TEOS aerogel are similar to those in the literature (Table 1) [43]. A shift in the band position corresponding to Si–O–Si (LO and TO mode), $\upsilon_B$ (Si–O), $\upsilon_S$ (Si–O) in all TEOS-POM hybrid catalysts are assigned at 1,230; 1,050; 960; and 795 cm$^{-1}$, respectively, thus confirming the immobilization of POMs as well as indicating a change in the chemical environment due to the silica-POMs linkage [10–12,33,42,44].

#### 3.1.2. Nitrogen adsorption–desorption study

The BET analysis in Fig. 2 shows the nitrogen adsorption–desorption isotherms for the obtained hybrid materials with hysteresis loops of type I and the isotherms of type IV. Moreover, the specific surface area varies between 250 and 900 m$^2$/g where the larger numbers lead to more efficient photocatalytic activity. Additionally, the pore size distribution was shown in Fig. 3 with a broad size distribution peak, and the total pore volume of materials fluctuates between 0.2 and 0.7 cm$^3$/g as summarized in Table 2. Also, the decrease in the specific surface area from free TEOS aerogels to hybrid TEOS-POMs as shown in Table 2 implies the successful immobilization and the pores' occupation by heteropolytungstates, where these results are in accordance with our previous work about the immobilization of POMs onto TEOS aerogels [33,41].

#### 3.1.3. SEM and EDX spectroscopy

The SEM in Fig. 4 shows the shape and morphology of the heteropolytungstate particles with a fine nanostructure which are aggregated into clusters due to the small dimensions of obtained particles. Furthermore, the SEM exposed the supported heteropolytungstates on the porous silica

Table 1
Characteristic vibration frequencies (cm$^{-1}$) in FTIR spectra of TEOS Aerogel and TEOS-POMs

|  | Vibrations (cm$^{-1}$) | | | |
|---|---|---|---|---|
| TEOS Aerogel | 1,230 | 1,050 | 960 | 795 |
| TEOS-PW$_9$ | 1,245 | 1,037 | 947 | 801 |
| TEOS-P$_2$W$_{12}$ | 1,230 | 1,083 | 917 | 797 |
| TEOS-P$_2$W$_{15}$ | 1,240 | 1,072 | 938 | 806 |
| TEOS-P$_2$W$_{18}$ | 1,240 | 1,038 | 963 | 798 |
| TEOS-P$_4$W$_{24}$ | 1,234 | 1,077 | 944 | 795 |
| TEOS-P$_5$W$_{30}$ | 1,235 | 1,029 | 953 | 795 |
| TEOS-P$_6$W$_{18}$ | 1,223 | 1,090 | 963 | 800 |
| TEOS-P$_8$W$_{48}$ | 1,239 | 1,050 | 950 | 802 |

Table 2
Data points of specific surface area (m$^2$/g), total pore volume (cm$^3$/g), volume of mesopores (cm$^3$/g), and volume of micropores (cm$^3$/g) for TEOS Aerogel and TEOS-POMs

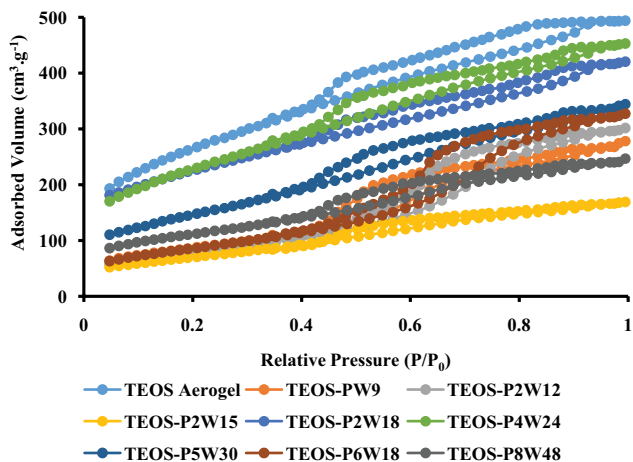|  | Specific surface area (m$^2$/g) | Total pore volume (cm$^3$/g) | Volume of mesopores (cm$^3$/g) | Volume of micropores (cm$^3$/g) |
|---|---|---|---|---|
| TEOS aerogel | 925 | 0.77 | 0.43 | 0.34 |
| TEOS-PW$_9$ | 308 | 0.43 | 0.40 | 0.02 |
| TEOS-P$_2$W$_{12}$ | 284 | 0.47 | 0.45 | 0.02 |
| TEOS-P$_2$W$_{15}$ | 254 | 0.26 | 0.21 | 0.06 |
| TEOS-P$_2$W$_{18}$ | 758 | 0.65 | 0.36 | 0.29 |
| TEOS-P$_4$W$_{24}$ | 796 | 0.70 | 0.41 | 0.28 |
| TEOS-P$_5$W$_{30}$ | 525 | 0.53 | 0.38 | 0.15 |
| TEOS-P$_6$W$_{18}$ | 308 | 0.51 | 0.49 | 0.02 |
| TEOS-P$_8$W$_{48}$ | 381 | 0.38 | 0.27 | 0.11 |

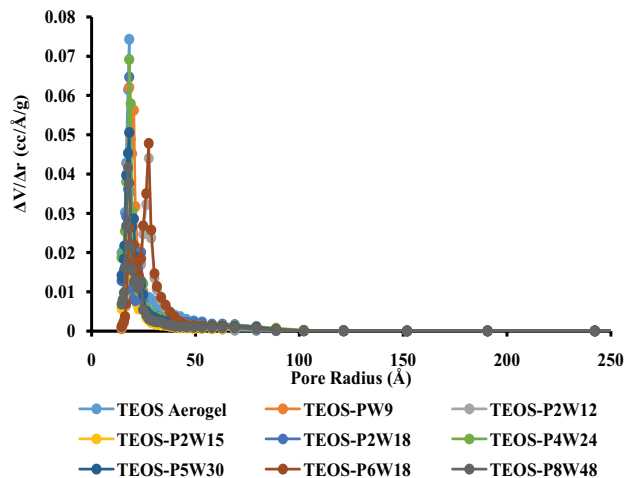Fig. 2. Nitrogen adsorption–desorption isotherms of TEOS Aerogel and TEOS-POMs.



Fig. 3. Pore size distribution of TEOS Aerogel and TEOS-POMs.

aerogels at the nanometer scale (500 nm). It is clearly evident that the morphology of the particles is heterogeneous in all cases, thus confirming the uniform distribution of POMs onto the silica aerogel pores. The elemental analysis of the hybrid materials was carried out by EDX on the SEM as shown in Table 3, the results confirmed that the composition of the hybrid materials was in accordance with the initial elemental composition without any impurities.

## 3.2. Thermal gravimetric analysis

The thermogravimetric analyses in Fig. 5 indicate that some POMs and TEOS-POMs exhibit two main weight loss steps. The TGA curves show the thermal stability withstands up to 1,000°C. Initially, in the range of 125°C–225°C contributes to the weight loss of 6%–14%, attributed to the release of coordinated and interstitial (non-coordinated) water molecules. The second weight loss step evident for some samples at approximately 1% in the range of 460°C–500°C represents the decomposition of the remaining structures (organic molecules).

## 3.3. X-ray diffraction

The experimental XRD patterns show that the positions of peaks are in good agreement with each other, thus
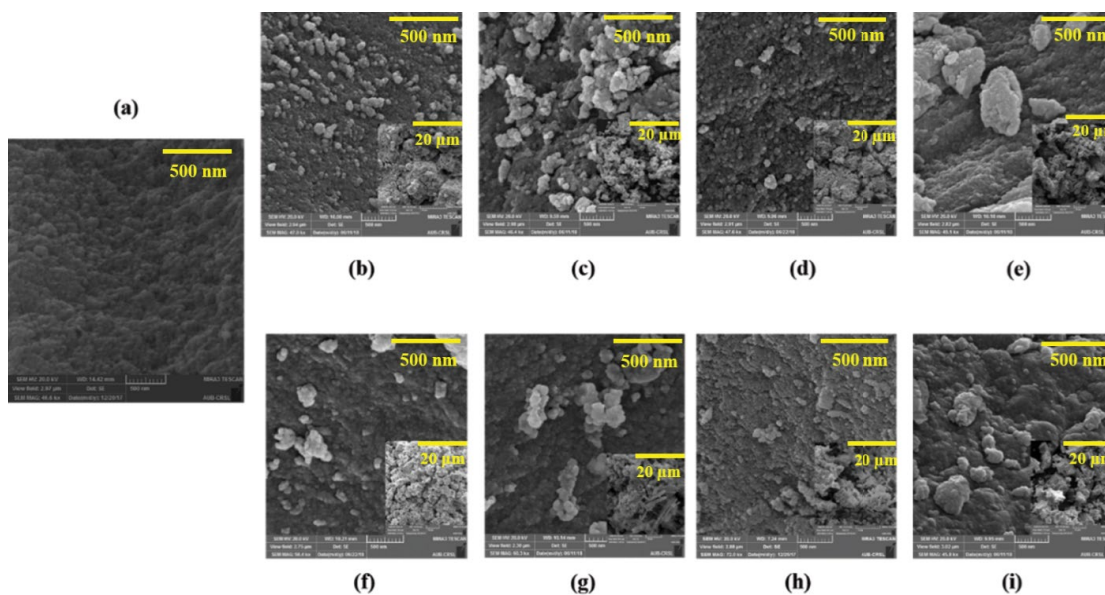


Fig. 4. SEM images of (a) TEOS aerogel, (b) TEOS-$PW_9$ at 500 nm and $PW_9$ at 20 μm, (c) TEOS-$P_2W_{12}$ at 500 nm and $P_2W_{12}$ at 20 μm, (d) TEOS-$P_2W_{15}$ at 500 nm and $P_2W_{15}$ at 20 μm, (e) TEOS-$P_2W_{18}$ at 500 nm and $P_2W_{18}$ at 20 μm, (f) TEOS-$P_4W_{24}$ at 500 nm and $P_4W_{24}$ at 20 μm, (g) TEOS-$P_5W_{30}$ at 500 nm and $P_5W_{30}$ at 20 μm, (h) TEOS-$P_6W_{18}$ at 500 nm and $P_6W_{18}$ at 20 μm, and (i) TEOS-$P_8W_{48}$ at 500 nm and $P_8W_{48}$ at 20 μm.

Table 3
EDX elemental analysis of the TEOS-POMs

| Weight % | C | O | Si | K | Na | P | W |
|----------|-------|-------|-------|------|------|------|-------|
| TEOS-PW$_9$ | 9.82 | 37.76 | 20.68 | – | 2.40 | 1.25 | 28.09 |
| TEOS-P$_2$W$_{12}$ | 10.44 | 37.50 | 22.97 | 3.78 | – | 1.15 | 29.31 |
| TEOS-P$_2$W$_{15}$ | 19.68 | 42.13 | 17.59 | – | 0.90 | 0.63 | 19.08 |
| TEOS-P$_2$W$_{18}$ | 24.82 | 38.59 | 30.06 | 0.17 | – | 1.21 | 5.17 |
| TEOS-P$_4$W$_{24}$ | 11.77 | 41.79 | 15.02 | 2.50 | – | 0.72 | 28.20 |
| TEOS-P$_5$W$_{30}$ | 32.13 | 40.30 | 8.06 | – | 0.33 | 4.05 | 15.13 |
| TEOS-P$_6$W$_{18}$ | 5.76 | 48.94 | 28.35 | – | 2.80 | 0.94 | 13.20 |
| TEOS-P$_8$W$_{48}$ | 9.40 | 49.28 | 29.50 | 0.77 | – | 0.44 | 10.61 |

showing similarity and phase purity. Also, the simulated XRD patterns of a pure TEOS aerogel, pure POMs, and the hybrid catalysts TEOS-POMs in Figs. S10–S17 show that some of the diffraction peaks indexed to POMs disappeared and the appearance of a broad peak around 2θ = 24° which is related to the amorphous silica aerogels in the case of TEOS-POM materials. All the variation in peaks revealed that a successful immobilization emerged in all TEOS-POM hybrid catalysts.

### 3.4. UV-Vis analysis and photocatalytic activity

It is widely known in the literature that POMs can be used as green photocatalysts for the treatment of water from organic pollutants [19–21]. The UV light irradiation induces POMs and TEOS-POMs to produce oxygen by excitation of electrons from the highest occupied molecular orbital (HOMO) to the lowest unoccupied molecular orbital (LUMO). The HOMO needs one electron from water molecules which gets oxygenated to form OH radicals in order to completely achieve the photocatalytic process [35,45,46].

Fig. 6 shows the spectra of MB solution during the photodegradation under UV light irradiation in the presence of 75 mg of POMs and TEOS-POM hybrid catalysts. The spectra confirm that the cationic MB molecules are preferentially adsorbed on TEOS-POMs and degraded on POMs. Moreover, the surface of the hybrid catalysts possessing a strongly negative charge absorbs the cationic MB molecules via electrostatic interactions.

Furthermore, the concentrations of MB ($C/C_0$) as a function of irradiation time in minutes were plotted in Fig. 7, where $C_0$ is the initial concentration of MB before the addition of catalysts. It is clearly seen that the absorbance of MB decreased obviously with time in all cases of catalysts with different photocatalytic efficiencies. An aliquot of the MB solution has been retrieved every 15 min for UV measurements, which resulted in 75%–95% degradation of MB for POMs and 90%–98% for TEOS-POMs.

The degradation results demonstrate that all POMs and TEOS-POM hybrid catalysts are good candidates and efficient photocatalysts for the degradation of MB. Additionally, the scrutinized experimental observations revealed that the color of MB changed from blue to light blue and then colorless after UV irradiation for 120 min, thus showing an almost complete degradation of MB. Moreover, the results
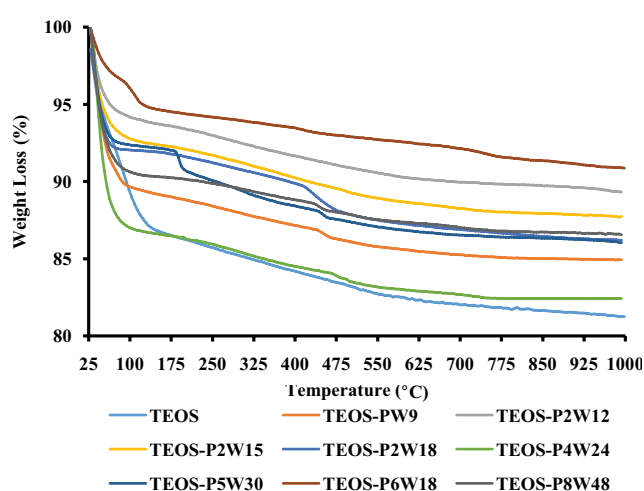


Fig. 5. Thermogravimetric analysis of TEOS Aerogel and TEOS-POMs.

indicate that the POMs and TEOS-POM hybrid catalysts have high selectivity towards MB degradation and are active in a relatively short period of time.

### 3.5. Intermediate products and mass spectra analysis of MB

The color of MB is dependent on two different factors, the chromophore group which is the conjugated system N–S at the central aromatic heterocycle, and the auxochrome group pertaining to the N-containing groups with lone pair electrons at the benzene ring [47]. In addition, the removal of MB during the photocatalytic process involves the adsorption as well as the degradation using the POMs. Based on the differences in color at the end of the photodegradation, accordingly two possible mechanisms were proposed for MB degradation.

Many peaks of different intensities are shown in the MS spectra in addition to the peak of MB, which indicates the variation in concentration and the composition of the products during the degradation. The intermediate products formed during the photocatalytic degradation reaction were detected and identified using MS equipped with an electrospray ionization at the positive ion mode. Various intermediate products were formed in all cases of POMs and TEOS-POMs as shown in Fig. 8 including
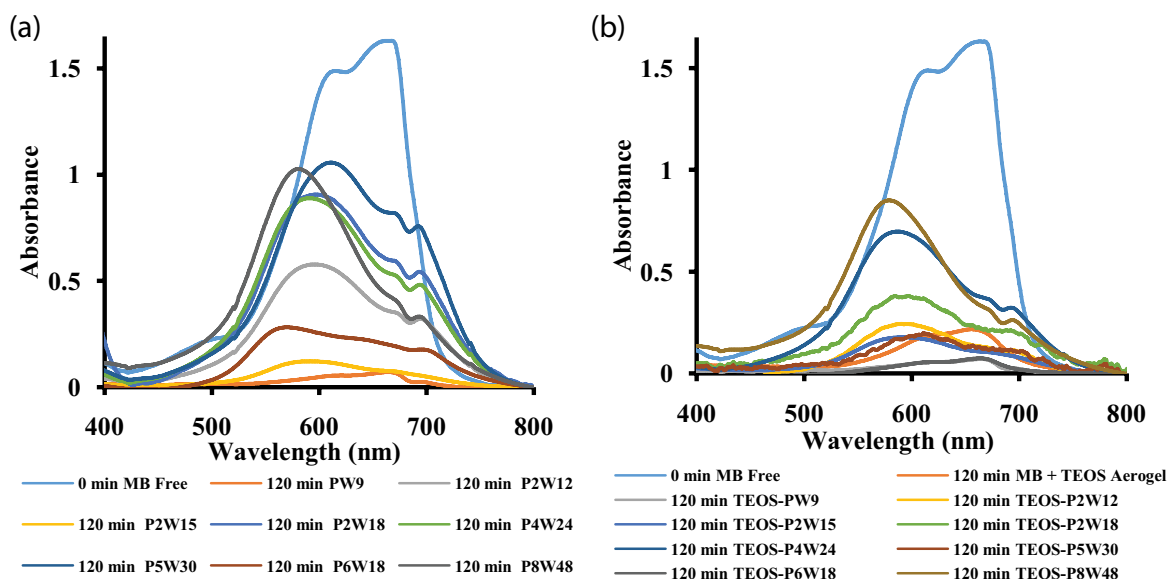
Fig. 6. Time dependent UV-Vis spectra of MB at 0 min without catalyst and 120 min with POMs (a), and at 0 min without catalyst, 120 min with TEOS Aerogel without catalyst, and 120 min with TEOS-POMs (b). [Dye] = $2.975 \times 10^{-5}$ M, catalyst amount = 75 mg, and temperature = 25°C.
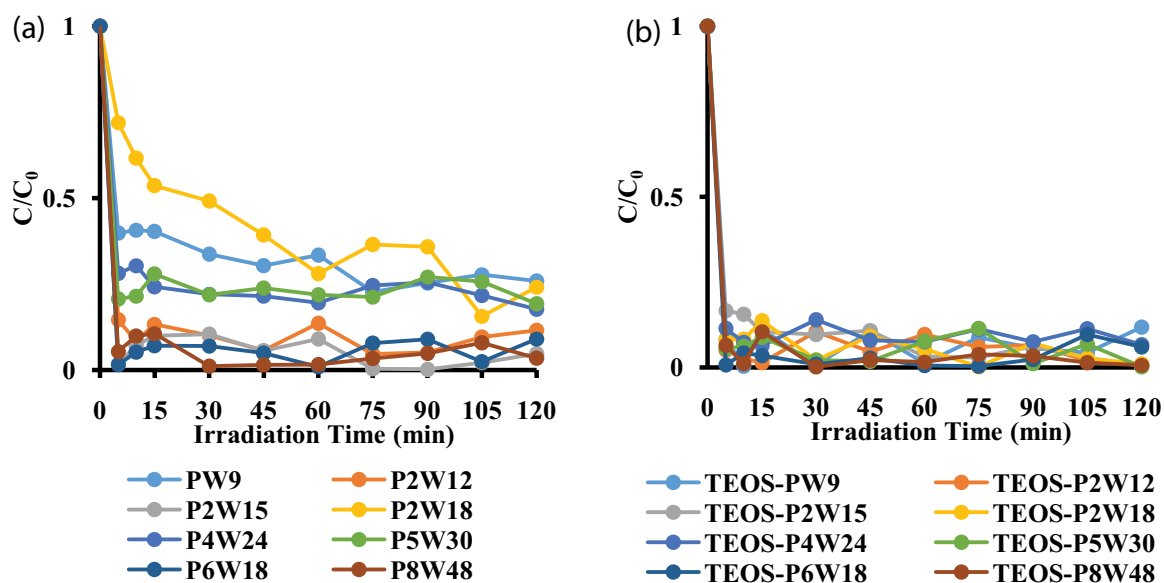


Fig. 7. Plot of $C/C_0$ of MB vs. irradiation time with POMs (a) and with TEOS-POMs (b).

2-amino-5-(methyl amino)-hydroxybenzene sulfonic acid ($m/z$ = 218), 2-amino-5-($N$-methyl formamide) benzene sulfonic acid ($m/z$ = 230), azure A ($m/z$ = 270), and azure B ($m/z$ = 256). Furthermore, azure A and azure B have been obtained by the demethylation cleavage as reported in the literature [48,49], the intermediate products are in agreement in terms of their masses with the eluted intermediates.

### 3.6. Effect of POM types

It was noticed in some cases, as shown in Fig. 9, that as the number of phosphorous atoms increase within the

POMs and TEOS-POMs, hence the percentage of removal efficiency in MB also increases. Moreover, it is evident that the MB degradation increases in efficiency going from $P_2W_{15}$ and TEOS-$P_2W_{15}$, then $P_6W_{18}$ and TEOS-$P_6W_{18}$, and then $P_8W_{48}$ and TEOS-$P_8W_{48}$. This increase in efficiency is due to the higher reactivity as well as the ease of assembly neutralized with counter cations similar to MB molecules in solution. Additionally, the primary structure leads to the formation of a secondary structure and then a tertiary structure thus acquiring more physical and chemical properties like porosity, particle size, and surface area [50].
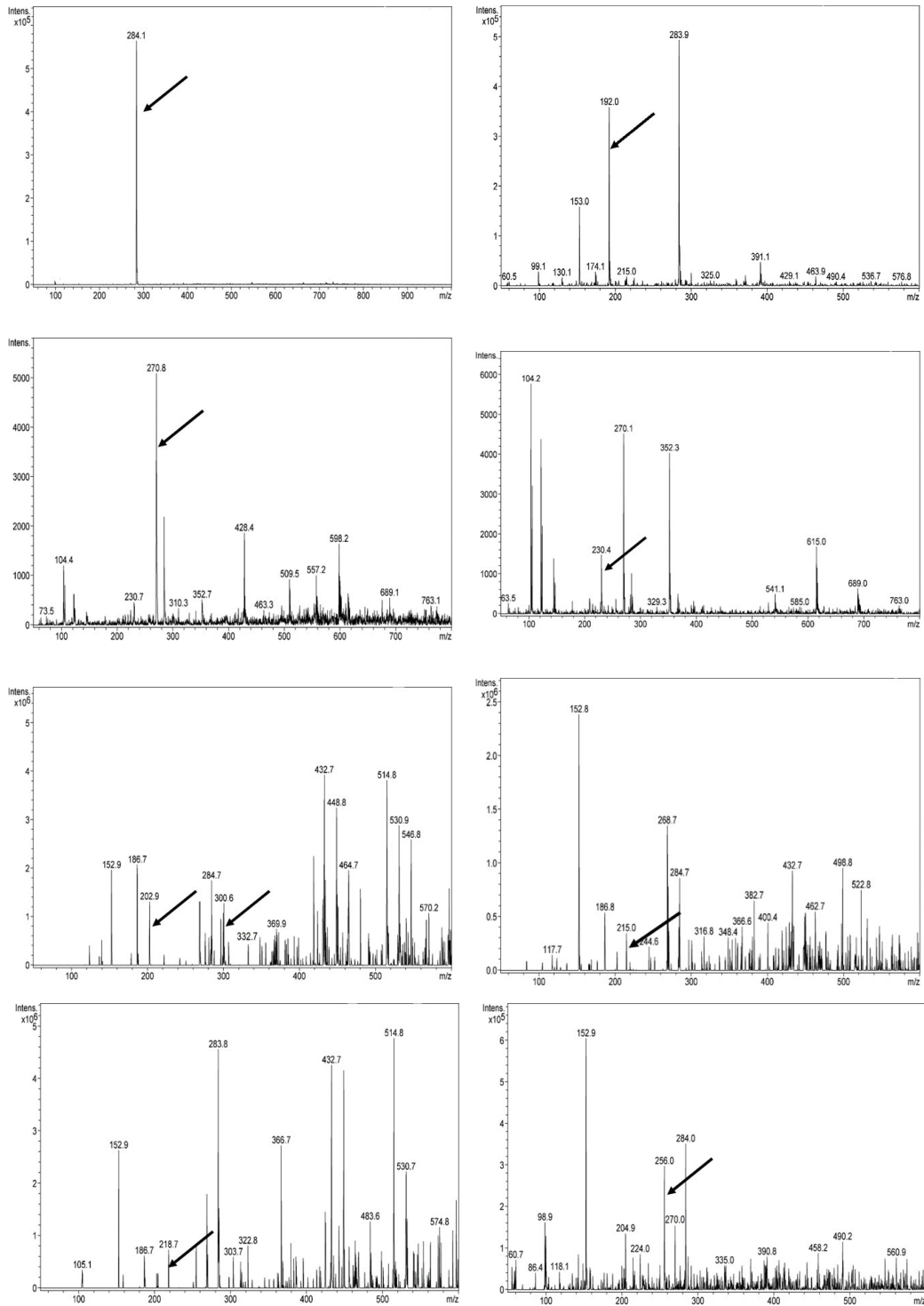
Fig. 8. Mass spectra of MB intermediates during photocatalytic degradation process.

## 4. Conclusion

In summary, the hybrid catalysts of TEOS-POMs have been successfully synthesized via a facile method, followed by full characterization using XRD, TGA, and IR to confirm purity as well as their chemical structure. The higher dispersion of immobilized POMs is confirmed by UV-Vis, BET, SEM, and EDX studies, which implies successful loading of POMs onto the network of the silica aerogels. The photocatalytic investigations of the hybrid catalysts show excellent activity towards the degradation of MB molecules
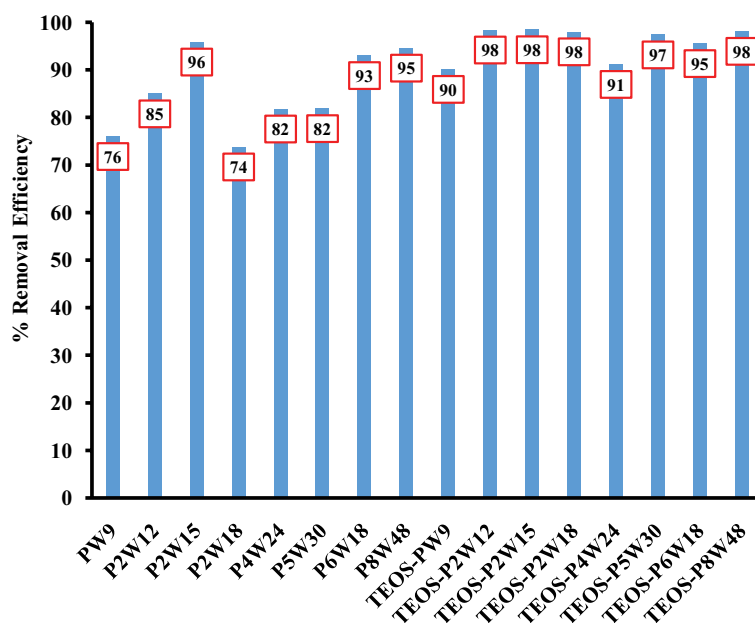
Fig. 9. Plot of the percentage removal efficiency of MB dye molecules with POMs and TEOS-POMs, under UV light.

under ultraviolet irradiation. The highest removal efficiency for MB was achieved between 75% and 98% in the first 15 min which readily remained constant after 120 min for POMs and POM-TEOS hybrids. Moreover, the formed intermediate products during the photocatalytic process were identified and confirmed by MS analyses.

### Acknowledgments

### References

[1] L.Y. Zhang, W. Zhang, Z. Zhou, C.M. Li, $\gamma$-Fe$_2$O$_3$ nanocrystals-anchored macro/meso-porous graphene as a highly efficient adsorbent toward removal of methylene blue, J. Colloid Interface Sci., 476 (2016) 200–205.

[2] J. Yang, R. Hu, W. Meng, Y. Du, A novel p-LaFeO$_3$/n-Ag$_3$PO$_4$ heterojunction photocatalyst for phenol degradation under visible light irradiation, Chem. Commun., 52 (2016) 2620–2623.

[3] V. Jabbari, J.M. Veleta, M. Zarei-Chaleshtori, J. Gardea-Torresdey, D. Villagrán, Green synthesis of magnetic MOF@GO and MOF@CNT hybrid nanocomposites with high adsorption capacity towards organic pollutants, Chem. Eng. J., 304 (2016) 774–783.

[4] H. Lachheb, E. Puzenat, A. Houas, M. Ksibi, E. Elaloui, C. Guillard, J.M. Herrmann, Photocatalytic degradation of various types of dyes (Alizarin S, Crocein Orange G, Methyl Red, Congo Red, Methylene Blue) in water by UV-irradiated titania, Appl. Catal., B, 39 (2002) 75–90.

[5] Y.H. Zhang, Z.R. Tang, X.Z. Fu, Y.J. Xu, TiO$_2$-graphene nanocomposites for gas-phase photocatalytic degradation of volatile aromatic pollutant: is TiO$_2$-graphene truly different from other TiO$_2$-carbon composite materials?, ACS Nano, 4 (2010) 7303–7314.

[6] L.C. Zhou, J.J. Ma, H. Zhang, Y.M. Shao, Y.F. Li, Fabrication of magnetic carbon composites from peanut shells and its application as a heterogeneous Fenton catalyst in removal of methylene blue, Appl. Surf. Sci., 324 (2015) 490–498.

[7] C.S. Castro, M.C. Guerreiro, L.C.A. OLiveira, M. Goncalves, A.S. Anastacio, M. Nazzarro, Iron oxide dispersed over activated carbon: support influence on the oxidation of the model molecule methylene blue, Appl. Catal., B, 367 (2009) 53–58.

[8] J.J. Ma, L.C. Zhou, W.F. Dan, H. Zhang, Y.M. Shao, C. Bao, L.Y. Jing, Novel magnetic porous carbon spheres derived from chelating resin as a heterogeneous Fenton catalyst for the removal of methylene blue from aqueous solution, J. Colloid Interface Sci., 446 (2015) 298–306.

[9] M.A. Rauf, M.A. Meetani, A. Khaleel, A. Ahmed, Photocatalytic degradation of Methylene Blue using a mixed catalyst and product analysis by LC/MS, Chem. Eng. J., 157 (2010) 373–378.

[10] R. Al-Oweini, B.S. Bassil, M. Itani, D.B. Emiroglu, U. Kortz, The mixed-valent 10-manganese(III/IV)-containing 36-tungsto-4-arsenate(V), [MnIII$_6$MnIV$_4$O$_4$(OH)$_{12}$(H$_2$O)$_{12}$(A-[$\beta$]-AsW$_9$O$_{34}$)$_4$]$^{22-}$, Acta Crystallogr., Sect. C: Struct. Chem., 74 (2018) 1390–1394.

[11] R. Al-Oweini, B.S. Bassil, J. Friedl, V. Kottisch, M. Ibrahim, M. Asano, B. Keita, G. Novitchi, Y. Lan, A. Powell, U. Stimming, U. Kortz, Synthesis and characterization of multinuclear manganese-containing tungstosilicates, Inorg. Chem., 53 (2014) 5663–5673.

[12] R. Al-Oweini, B.S. Bassil, T. Palden, B. Keita, Y. Lan, A.K. Powell, U. Kortz, The manganese(III)-containing tungstophosphate [Mn$^{III}$$_3$(H$_2$O)$_5$(A-$\alpha$-PW$_9$O$_{34}$)$_2$]$^{9-}$, Polyhedron, 52 (2013) 461–466.

[13] L.F. Piedra-Garza, M. Barsukova-Stuckart, B.S. Bassil, R. Al-Oweini, U. Kortz, Diethyltin-containing tungstoarsenate(V), [{Sn(C$_2$H$_5$)$_2$}$_3$(H$_2$O)$_6$(A-$\alpha$-As$^V$W$_9$O$_{34}$)]$^{3-}$, J. Cluster Sci., 23 (2012) 939–951.

[14] B.S. Bassil, M. Ibrahim, R. Al-Oweini, M. Asano, Z. Wang, J. Van Tol, N.S. Dalal, K.Y. Choi, R. Ngo Biboum, B. Keita, L. Nadjo, U. Kortz, A planar {Mn$_{19}$(OH)$_{12}$}$^{26+}$ unit incorporated in a 60-tungsto-6-silicate polyanion, Angew. Chem. Int. Ed. Engl., 50 (2011) 5961–5964.

[15] W. Liu, R. Al-Oweini, K. Meadows, B.S. Bassil, Z. Lin, J.H. Christian, N.S. Dalal, A.M. Bossoh, I.M. Mbomekallé, P. De Oliveira, J. Iqbal, U. Kortz, Cr$^{III}$-substituted heteropoly-16-tungstates [Cr$^{III}$$_2$(B-$\beta$-X$^{IV}$W$_8$O$_{31}$)$_2$]$^{14-}$ (X = Si, Ge): magnetic, biological, and electrochemical studies, Inorg. Chem., 55 (2016) 10936–10946.

[16] W. Liu, Z. Lin, B.S. Bassil, R. Al-Oweini, U. Kortz, Synthesis and structure of hexatungstochromate(III), $[H_3Cr^{III}W_6O_{24}]^6$, Chimia, 69 (2015) 537–540.

[17] W. Liu, J.H. Christian, R. Al-Oweini, B.S. Bassil, J. Van Tol, M. Atanasov, F. Neese, N.S. Dalal, U. Kortz, Synthesis, detailed characterization, and theoretical understanding of mononuclear chromium(III)-containing polyoxotungstates $[Cr^{III}(HX^VW_7O_{28})_2]^{13-}$ (X = P, As) with exceptionally large magnetic anisotropy, Inorg. Chem., 53 (2014) 9274–9283.

[18] S. Farhadi, F. Mahmoudi, M.M. Amini, M. Dusek, M. Jarosova, Synthesis and characterization of a series of novel perovskite-type $LaMnO_3$/Keggin-type polyoxometalate hybrid nanomaterials for fast and selective removal of cationic dyes from aqueous solutions, Dalton Trans., 46 (2017) 3252–3264.

[19] L. Youssef, G. Younes, R. Al-Oweini, Photocatalytic degradation of atrazine by heteropolyoxotungstates, J. Taibah Univ. Sci., 13 (2019) 274–279.

[20] L. Youssef, H. El-Rassy, G. Younes, R. Al-Oweini, Photocatalytic and kinetic study on the degradation of three food pesticides using vanadium-substituted polyoxotungstates, Int. J. Environ. Res., 13 (2019) 899–907.

[21] F. Yahya, H. El-Rassy, G. Younes, R. Al-Oweini, Synthesis and characterisation of mesoporous hybrid silica-polyoxometalate aerogels for photocatalytic degradation of rhodamine B and methylene blue, Int. J. Environ. Anal. Chem., 99 (2019) 1375–1396.

[22] N. El Ghouch, R. Al-Oweini, R. Awad, Preparation and physical properties of $(Bi_{1.8}Pb_{0.4})Sr_2Ca_3Cu_5O_{10+\delta}$ superconductors impregnated with mangano(II)undecatungstosilicate nanomaterials, Appl. Phys. A, 854 (2019) 1–11.

[23] N. El Ghouch, R. Al-Oweini, R. Awad, Synthesis, characterization and electrical properties of hybrid mono-iron-substituted undecatungstosilicate/(Bi,Pb)-2223 phase superconductors, Mater. Res. Express, 6 (2019) 116001, doi: 10.1088/2053-1591/ab46e2.

[24] M. Natali, I. Bazzan, S. Goberna-Ferrón, R. Al-Oweini, M. Ibrahim, B.S. Bassil, H. Dau, F. Scandola, J.R. Galán-Mascarós, U. Kortz, A. Sartorel, I. Zaharieva, M. Bonchio, Photo-assisted water oxidation by high-nuclearity cobalt-oxo cores: tracing the catalyst fate during oxygen evolution turnover, Green Chem., 19 (2017) 2416–2426.

[25] H.Y. Chen, R. Al-Oweini, J. Friedl, C.Y. Lee, L. Li, U. Kortz, U. Stimming, M. Srinivasan, A novel SWCNT-polyoxometalate nanohybrid material as an electrode for electrochemical supercapacitors, Nanoscale, 7 (2015) 7934–7941.

[26] A. Bijelic, C. Molitor, S.G. Mauracher, R. Al-Oweini, U. Kortz, A. Rompel, Hen egg-white lysozyme crystallisation: protein stacking and structure stability enhanced by a tellurium(VI)-centred polyoxotungstate, ChemBioChem, 16 (2015) 233–241.

[27] S.G. Mauracher, C. Molitor, R. Al-Oweini, U. Kortz, A. Rompel, Crystallization and preliminary X-ray crystallographic analysis of latent isoform PPO4 mushroom (*Agaricus bisporus*) tyrosinase, Acta Crystallogr., Sect. F: Struct. Biol. Commun., 70 (2014) 263–266.

[28] S.G. Mauracher, C. Molitor, R. Al-Oweini, U. Kortz, A. Rompel, Latent and active abPPO4 mushroom tyrosinase cocrystallized with hexatungstotellurate(VI) in a single crystal, Acta Crystallogr., Sect. D: Biol. Crystallogr., 70 (2014) 2301–2315.

[29] Z. Ilyas, H.S. Shah, R. Al-Oweini, U. Kortz, J. Iqbal, Antidiabetic potential of polyoxotungstates: *In vitro* and *in vivo* studies, Metallomics, 6 (2014) 1521–1526.

[30] J. Friedl, R. Al-Oweini, M. Herpich, B. Keita, U. Kortz, U. Stimming, Electrochemical studies of tri-manganese substituted Keggin polyoxoanions, Electrochim. Acta, 141 (2014) 357–366.

[31] H.Y. Chen, G. Wee, R. Al-Oweini, J. Friedl, K.S. Tan, Y. Wang, C.L. Wong, U. Kortz, U. Stimming, M. Srinivasan, A polyoxovanadate as an advanced electrode material for supercapacitors, ChemPhysChem, 15 (2014) 2162–2169.

[32] R. Al-Oweini, A. Sartorel, B.S. Bassil, M. Natali, S. Berardi, F. Scandola, U. Kortz, M. Bonchio, Photocatalytic water oxidation by a mixed-valent $Mn^{III}_3Mn^{IV}O_3$ manganese oxo core that mimics the natural oxygen-evolving center, Angew. Chem. Int. Ed. Engl., 53 (2014) 11182–11185.

[33] R. Al-Oweini, S. Aghyarian, H. El-Rassy, Immobilized polyoxometalates onto mesoporous organically-modified silica aerogels as selective heterogeneous catalysts of anthracene oxidation, J. Sol-Gel Sci. Technol., 61 (2012) 541–550.

[34] L. Zhang, B. Shan, H. Yang, D. Wu, R. Zhu, J. Niea, R. Cao, A new heterogeneous photocatalyst based on Wells–Dawson polyoxometalate and nickel coordination compounds: synthesis, structure and property, RSC Adv., 5 (2015) 23556–23562.

[35] A. Dolbecq, P. Mialane, B. Keitab, L. Nadjo, Polyoxometalate-based materials for efficient solar and visible light harvesting: application to the photocatalytic degradation of azo dyes, J. Mater. Chem., 22 (2012) 24509–24521.

[36] R. Sivakumar, J. Thomas, M. Yoon, Polyoxometalate-based molecular/nano composites: advances in environmental remediation by photocatalysis and biomimetic approaches to solar energy conversion, J. Photochem. Photobiol., C, 13 (2012) 277–298.

[37] X. Qu, Y. Guo, C. Hu, Preparation and heterogeneous photocatalytic activity of mesoporous $H_3PW_{12}O_{40}/ZrO_2$ composites, J. Mol. Catal. A: Chem., 262 (2007) 128–135.

[38] C. Zhan, M. Zhong, F. Chen, J. Yang, X. Cao, X. Jiang, Decolorization of rhodamine B using hydrogen peroxide and $H_3PW_{12}O_{40}@C$ photocatalyst synthesized in situ under ultraviolet irradiation, Desal. Water Treat., 53 (2015) 2970–2979.

[39] A.P. Ginsberg, Inorganic Syntheses, Wiley-Interscience, New York, 1990.

[40] E.O. North, Inorganic Syntheses, The McGraw-Hill Book Company, Inc., New York, NY, 1939.

[41] R. Al-Oweini, H. El-Rassy, Surface characterization by nitrogen adsorption of silica aerogels synthesized from various $Si(OR)_4$ and $R''Si(OR')_3$ precursors, Appl. Surf. Sci., 257 (2010) 276–281.

[42] R. Al-Oweini, H. El-Rassy, Synthesis and characterization by FTIR spectroscopy of silica aerogels prepared using several $Si(OR)_4$ and $R''Si(OR')_3$ precursors, J. Mol. Struct., 919 (2009) 140–145.

[43] J. Zhang, W.L. Chen, E.B. Wang, Synthesis and catalytic properties of novel $POM@TiO_2$ composite materials, Inorg. Chem. Commun., 38 (2013) 96–99.

[44] D. Kumar, C. Landry, Immobilization of a Mo,V-polyoxometalate on cationically modified mesoporous silica: Synthesis and characterization studies, Microporous Mesoporous Mater., 98 (2007) 309–316.

[45] A. Hiskia, A. Mylonas, E. Papaconstantinou, Comparison of the photoredox properties of polyoxometallates and semi-conducting particles, Chem. Soc. Rev., 30 (2001) 62–69.

[46] J.W. Sun, M.T. Li, J.Q. Sha, P.F. Yan, C. Wang, S.X. Li, Y. Pan, Assembly of the first polyoxometalate-based hybrid with [ring+helix] channels and photocatalytic activity, CrystEngComm, 15 (2013) 10584–10589.

[47] M.A. Sanroman, M. Pazos, M.T. Ricart, C. Cameselle, Electrochemical decolourisation of structurally different dyes, Chemosphere, 57 (2004) 233–239.

[48] C. Yogi, K. Kojima, N. Wada, H. Tokumoto, T. Takai, T. Mizoguchi, H. Tamiaki, Photocatalytic degradation of methylene blue by $TiO_2$ film and Au particles-$TiO_2$ composite film, Thin Solid Films, 516 (2008) 5881–5884.

[49] A. Orendorz, C. Ziegler, H. Gnaser, Photocatalytic decomposition of methylene blue and 4-chlorophenol on nanocrystalline $TiO_2$ films under UV illumination: a ToF-SIMS study, Appl. Surf. Sci., 255 (2008) 1011–1014.

[50] T. Okuhara, N. Mizuno, N. Misono, Advances in catalysis, Adv. Catal., 41 (1996) 113.

**Supporting information**

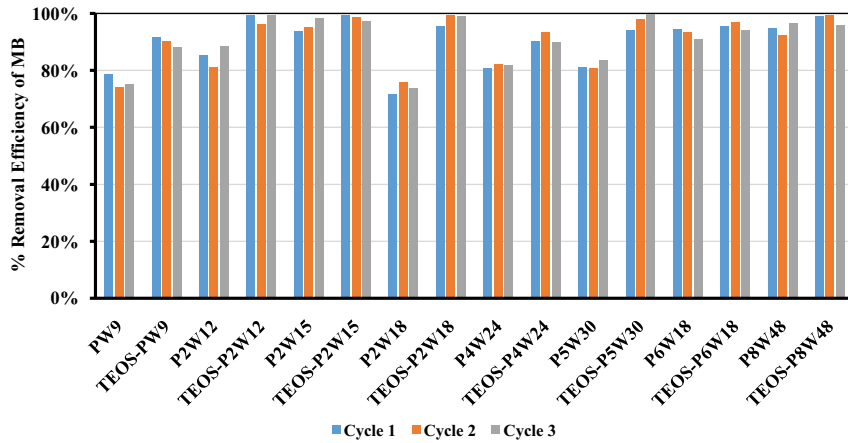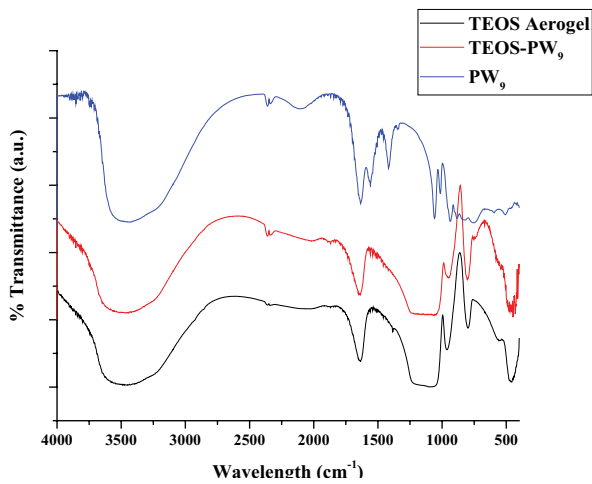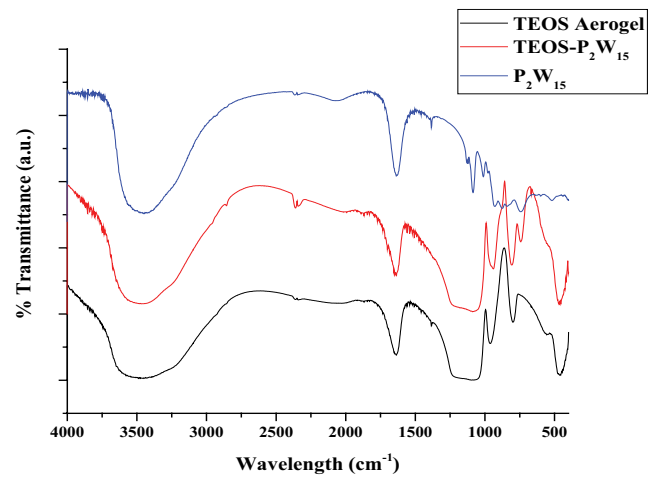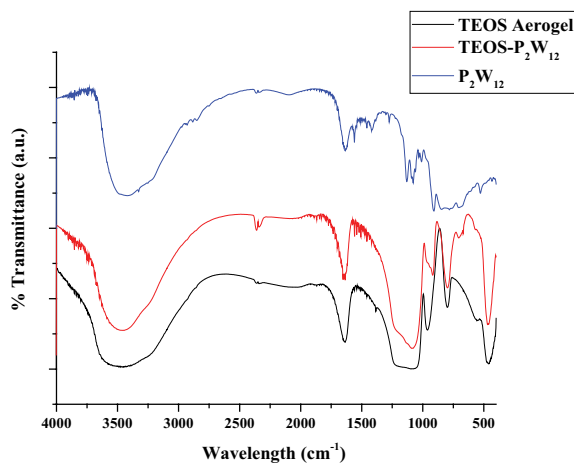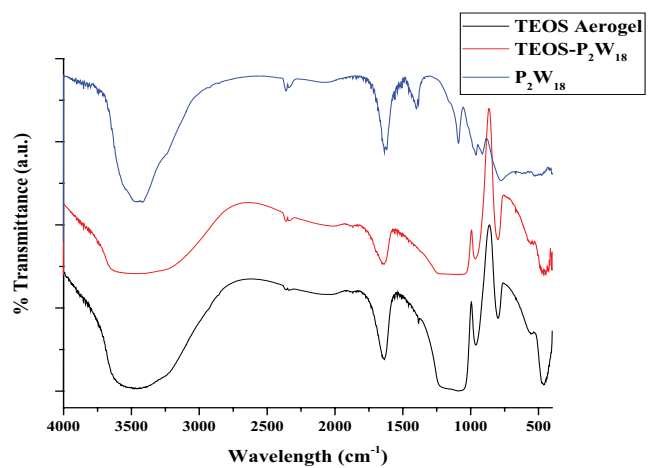**S1. Percentage of removal efficiency of MB at three cycles**



Fig. S1. Plot of removal efficiency percentage of MB of all POMs and TEOS-POMs at three cycles.

**S2. FTIR spectroscopy**



Fig. S2. FTIR spectra of TEOS aerogel, TEOS-$PW_9$, and $PW_9$.



Fig. S4. FTIR spectra of TEOS aerogel, TEOS-$P_2W_{15}$, and $P_2W_{15}$.



Fig. S3. FTIR spectra of TEOS aerogel, TEOS-$P_2W_{12}$, and $P_2W_{12}$.



Fig. S5. FTIR spectra of TEOS aerogel, TEOS-$P_2W_{18}$, and $P_2W_{18}$.
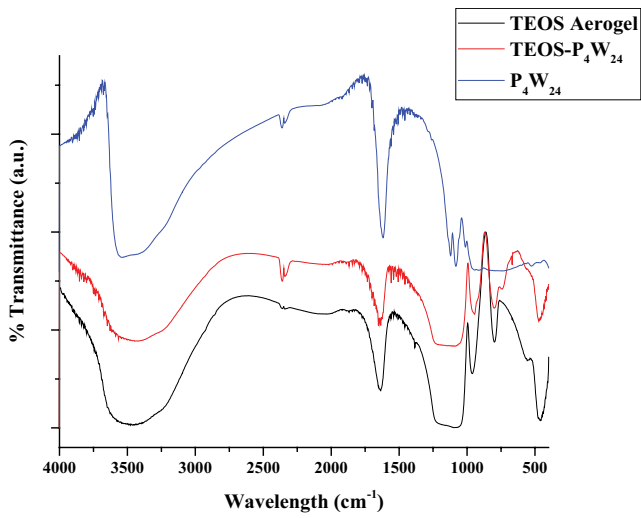
**X-ray diffraction**



Fig. S6. FTIR spectra of TEOS aerogel, TEOS-$P_4W_{24}$, and $P_4W_{24}$.
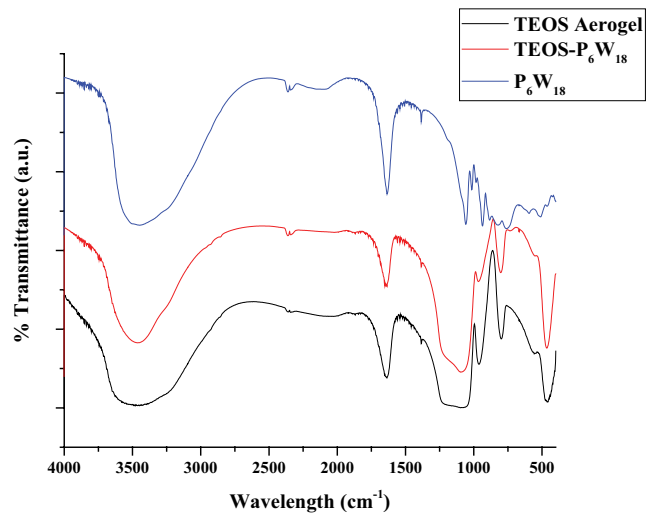


Fig. S9. FTIR spectra of TEOS aerogel, TEOS-$P_8W_{48}$, and $P_8W_{48}$.
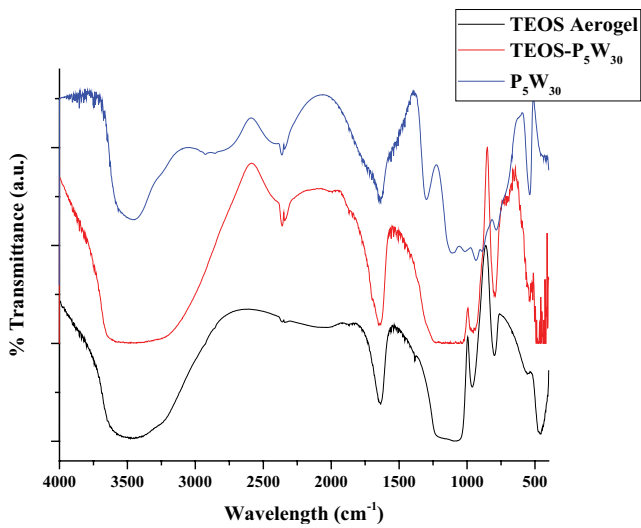


Fig. S7. FTIR spectra of TEOS aerogel, TEOS-$P_5W_{30}$, and $P_5W_{30}$.
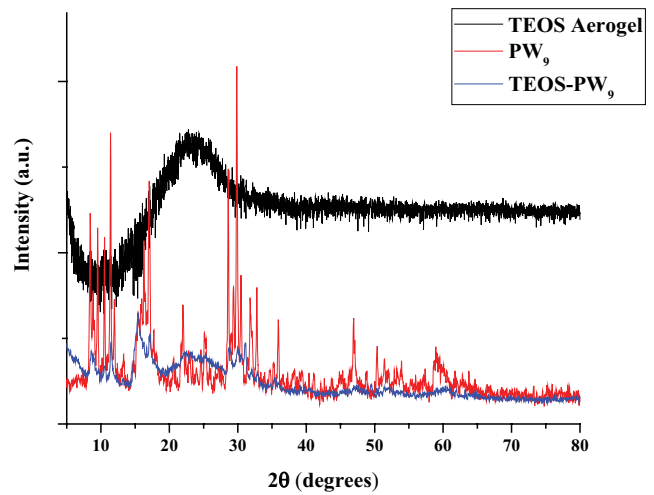


Fig. S10. XRD patterns of TEOS aerogel, $PW_9$, and TEOS-$PW_9$.
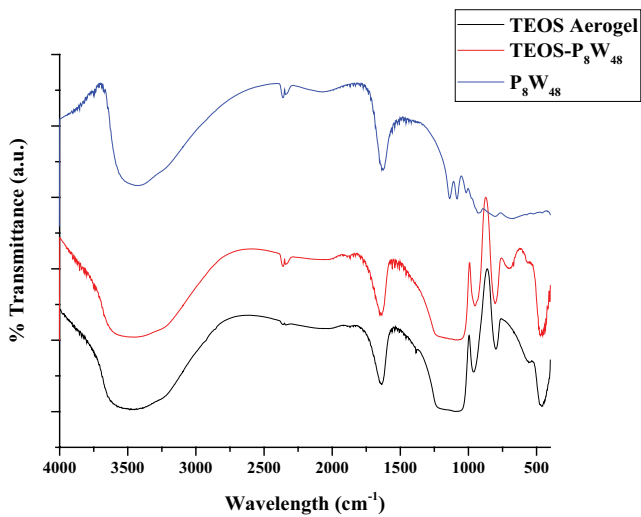


Fig. S8. FTIR spectra of TEOS aerogel, TEOS-$P_6W_{18}$, and $P_6W_{18}$.
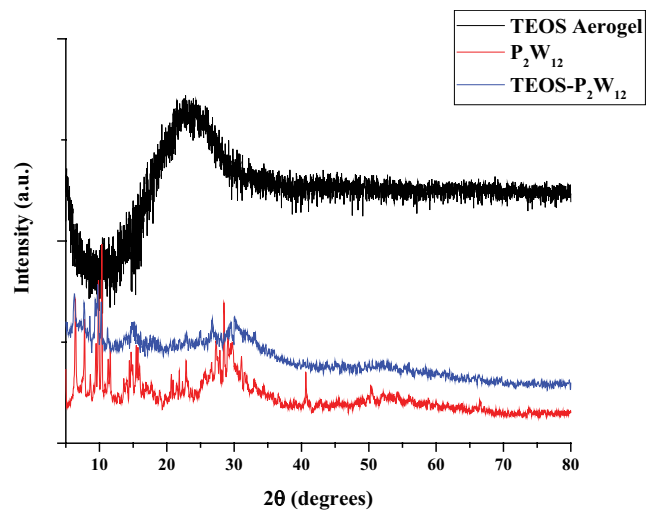


Fig. S11. XRD patterns of TEOS aerogel, $P_2W_{12}$, and TEOS-$P_2W_{12}$.
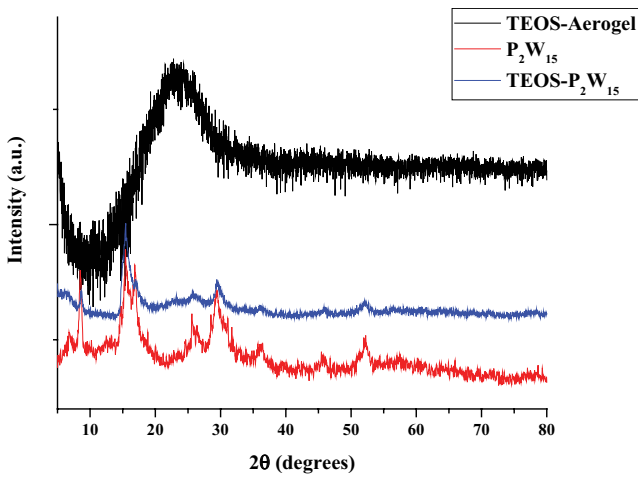
Fig. S12. XRD patterns of TEOS aerogel, $P_2W_{15}$, and TEOS-$P_2W_{15}$.
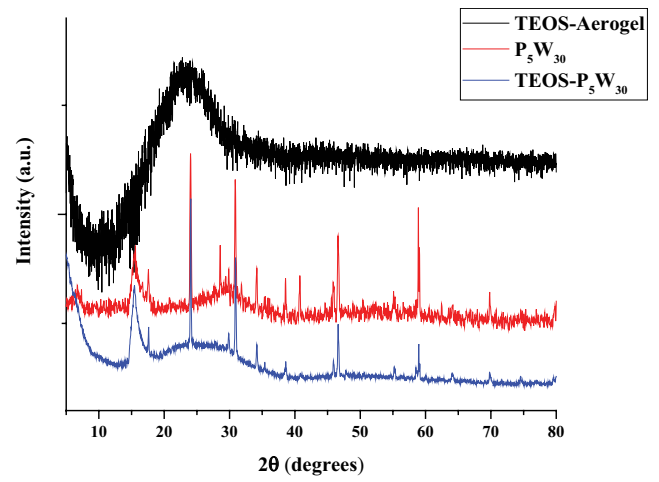


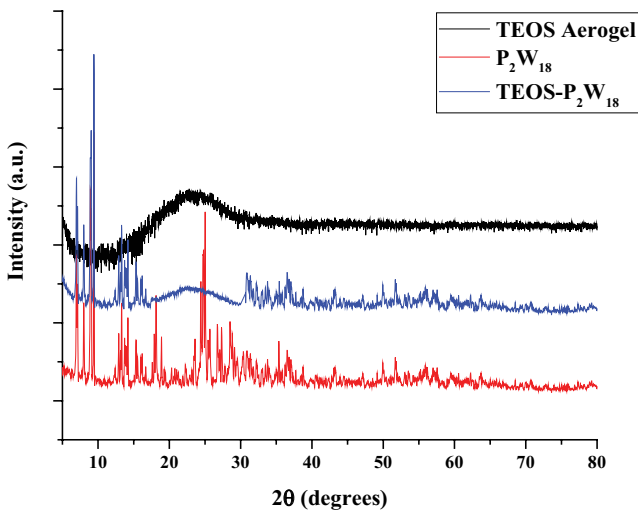Fig. S15. XRD patterns of TEOS aerogel, $P_5W_{30}$, and TEOS-$P_5W_{30}$.



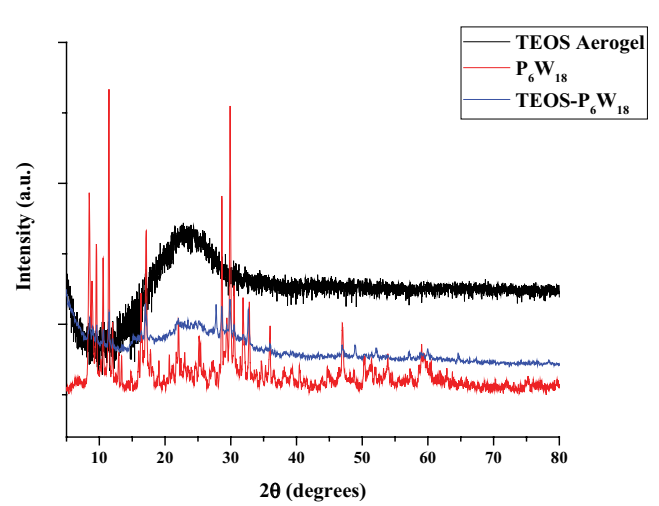Fig. S13. XRD patterns of TEOS aerogel, $P_2W_{18}$, and TEOS-$P_2W_{18}$.



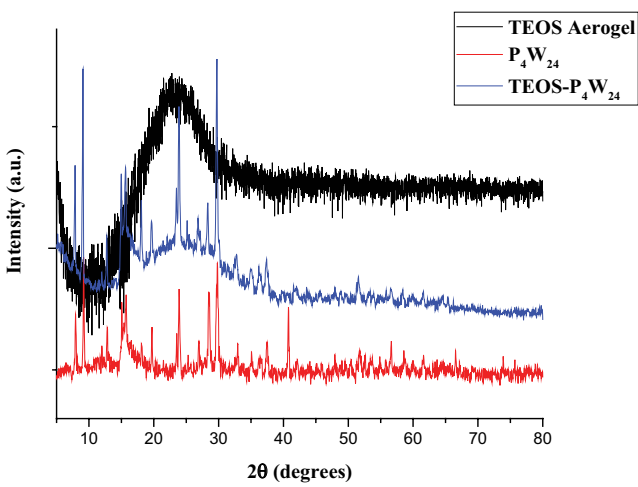Fig. S16. XRD patterns of TEOS aerogel, $P_6W_{18}$, and TEOS-$P_6W_{18}$.



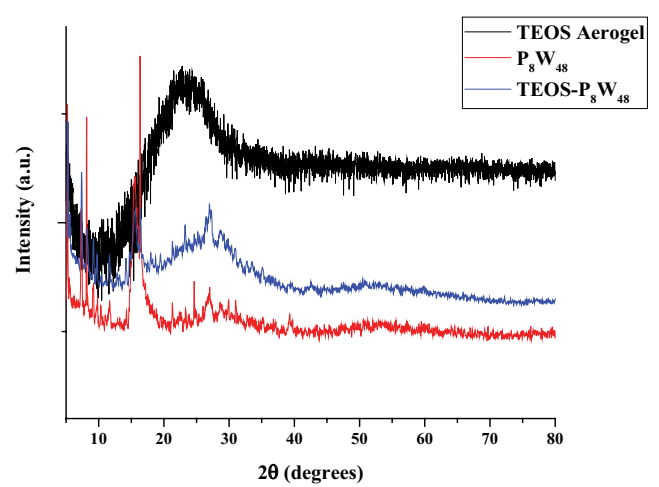Fig. S14. XRD patterns of TEOS aerogel, $P_4W_{24}$, and TEOS-$P_4W_{24}$.



Fig. S17. XRD patterns of TEOS aerogel, $P_8W_{48}$, and TEOS-$P_8W_{48}$.

Table S1
Removal efficiency percentage of POMs and TEOS-POMs at three cycles and their average

| | Cycle 1 (%) | Cycle 2 (%) | Cycle 3 (%) | Average (%) |
|---|---|---|---|---|
| $PW_9$ | 79 | 74 | 75 | 76 |
| TEOS-$PW_9$ | 92 | 90 | 88 | 90 |
| $P_2W_{12}$ | 85 | 81. | 88 | 85 |
| TEOS-$P_2W_{12}$ | 99 | 96 | 99 | 98 |
| $P_2W_{15}$ | 94 | 95 | 98 | 96 |
| TEOS-$P_2W_{15}$ | 99 | 99 | 97 | 98 |
| $P_2W_{18}$ | 72 | 76 | 74 | 74 |
| TEOS-$P_2W_{18}$ | 95 | 99 | 99 | 98 |
| $P_4W_{24}$ | 81 | 82 | 82 | 82 |
| TEOS-$P_4W_{24}$ | 90 | 93 | 90 | 91 |
| $P_5W_{30}$ | 81 | 81 | 83 | 82 |
| TEOS-$P_5W_{30}$ | 94 | 98 | 100 | 97 |
| $P_6W_{18}$ | 95 | 93 | 91 | 93 |
| TEOS-$P_6W_{18}$ | 95 | 97 | 94 | 95 |
| $P_8W_{48}$ | 95 | 92 | 97 | 95 |
| TEOS-$P_8W_{48}$ | 99 | 99 | 96 | 98 |